

Low-Temperature Graphene-Based Paste for Large-Area Carbon Perovskite Solar Cells

Paolo Mariani, Leyla Najafi, Gabriele Bianca, Marilena Isabella Zappia, Luca Gabatel, Antonio Agresti, Sara Pescetelli, Aldo Di Carlo,* Sebastiano Bellani,* and Francesco Bonaccorso*



Cite This: <https://doi.org/10.1021/acsami.1c02626>



Read Online

ACCESS |



Metrics & More



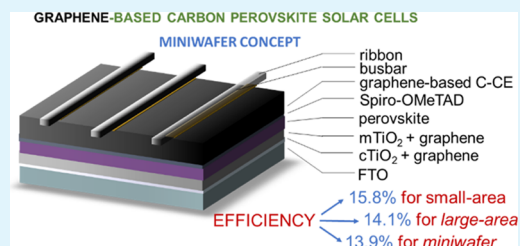
Article Recommendations



Supporting Information

ABSTRACT: Carbon perovskite solar cells (C-PSCs), using carbon-based counter electrodes (C-CEs), promise to mitigate instability issues while providing solution-processed and low-cost device configurations. In this work, we report the fabrication and characterization of efficient paintable C-PSCs obtained by depositing a low-temperature-processed graphene-based carbon paste atop prototypical mesoscopic and planar n-i-p structures. Small-area (0.09 cm²) mesoscopic C-PSCs reach a power conversion efficiency (PCE) of 15.81% while showing an improved thermal stability under the ISOS-D-2 protocol compared to the reference devices based on Au CEs. The proposed graphene-based C-CEs are applied to large-area (1 cm²) mesoscopic devices and low-temperature-processed planar n-i-p devices, reaching PCEs of 13.85 and 14.06%, respectively. To the best of our knowledge, these PCE values are among the highest reported for large-area C-PSCs in the absence of back-contact metallization or additional stacked conductive components or a thermally evaporated barrier layer between the charge-transporting layer and the C-CE (strategies commonly used for the record-high efficiency of C-PSCs). In addition, we report a proof-of-concept of metallized miniwafer-like area C-PSCs (substrate area = 6.76 cm², aperture area = 4.00 cm²), reaching a PCE on active area of 13.86% and a record-high PCE on aperture area of 12.10%, proving the metallization compatibility with our C-PSCs. Monolithic wafer-like area C-PSCs can be feasible all-solution-processed configurations, more reliable than prototypical perovskite solar (mini)modules based on the serial connection of subcells, since they mitigate hysteresis-induced performance losses and hot-spot-induced irreversible material damage caused by reverse biases.

KEYWORDS: perovskite solar cells, carbon, graphene, paintable, solution processing, large-area, scalability, metallization



INTRODUCTION

Perovskite solar cells (PSCs) are continuously attracting extensive attention among the photovoltaic (PV) technologies due to their low-cost solution processability¹ accompanied by outstanding performances, which reached certified power conversion efficiencies (PCEs) above 25% (record-high value of 25.5%).^{2–4} These values are strongly competitive with the PCEs of monocrystalline and heterojunction (HJT) silicon solar cells (26.1 and 26.7%, respectively)² and overpass certified ones of mass-affordable thin-film PV technologies, that is, copper indium gallium selenide and CdTe solar cells (23.4 and 22.1%, respectively).² Even more, perovskite-based tandem configurations, especially perovskite-silicon tandem solar cells, have achieved a certified PCE of 29.1%, thus enabling a cost-effective tandem roadmap for the silicon-PV industry.⁵ Nevertheless, the commercialization of the most efficient PSC forms is facing technical barriers,^{6,7} which mainly relates to the following: (1) the instability of the photoactive perovskite^{8,9} and charge-transporting layers (CTLs)⁹ and (2) the use of expensive, vacuum thermally evaporated noble metal-based back counter electrodes (CEs), for example, gold (Au) and silver (Ag).¹⁰ The chemical reactions between the perovskite layer and the CE through the migration of iodine

species or metal atoms are also further causes of material instability in assembled devices.^{11,12} Therefore, the research community is struggling to design novel efficient and stable perovskites, CTLs, interlayers, and metal-free CEs, which mitigate the above issues while providing cost-effective, large-area processability.¹ It is noteworthy that pressure-tight polymer (polyisobutylene)/glass stack encapsulation has been recently reported to prevent moisture intake while suppressing the outgassing of perovskite decomposition products.¹³ Consequently, the decomposition reaction for a prototypical triple cation perovskite [Cs_{0.05}FA_{0.8}MA_{0.15}Pb(I_{0.85}Br_{0.15})₃] was blocked, allowing the PSCs to pass the International Electrotechnical Commission (IEC) 61215:2016 Damp Heat and Humidity Freeze tests. Prospectively, if an appropriate encapsulation would stabilize PSCs, the replacement of noble metal-based CEs would acquire even more

Received: February 7, 2021

Accepted: April 26, 2021

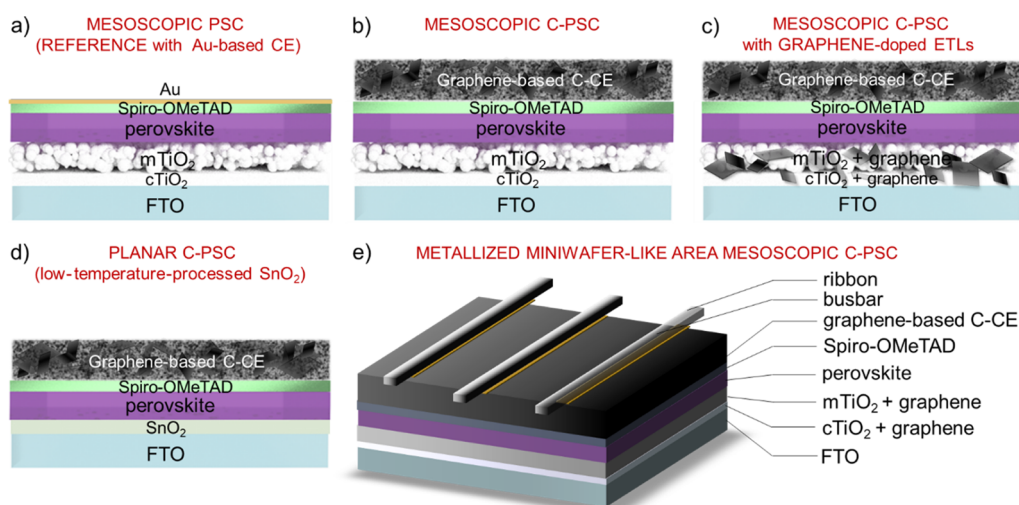


Figure 1. Schematics of the investigated n-i-p device architectures: (a) mesoscopic PSC (reference cell using Au-based CE); (b) mesoscopic C-PSCs based on graphene-based C-CE; (c) mesoscopic C-PSCs with graphene-doped ETLs (cTiO₂ + graphene and mTiO₂ + graphene); (d) planar C-PSC based on low-temperature-processed SnO₂ ETL; and (e) metallized miniwafer-like area mesoscopic C-PSCs, conceived as a replacement of the serial PSM configuration for the fabrication of reliable perovskite solar panels.

63 importance to achieve an estimated leveled cost of energy
 64 (LCOE) of perovskite solar panels of less than 5 US cents kW
 65 h⁻¹.^{10,14} Such a LCOE would be comparable or even inferior
 66 to the ones of commercially available silicon and thin-film-
 67 based solar PVs^{10,14} and competitive with the LCOEs of fossil
 68 fuels.¹⁵ In this context, carbon-based CEs (C-CEs) emerged as
 69 low-cost printable alternatives to Au- and Ag-based ones,
 70 leading to the so-called carbon-based PSCs (C-PSCs).^{16,17}
 71 Besides, the C-PSCs have the potential to minimize the CO₂
 72 footprint of PSC materials and manufacturing processes,^{17,18}
 73 paving the way for next-generation solar cells with the lowest
 74 environmental harm.
 75 Three types of C-PSCs have been classified, namely,
 76 mesoporous,^{19,20} embedment,^{21,22} and paintable C-PSCs.^{23,24}
 77 In the former, porous carbon electrodes are first deposited, and
 78 the perovskite precursor solution is infiltrated inside.^{19,20}
 79 Alternatively, the porous carbon electrode can be deposited
 80 onto a perovskite precursor (e.g., PbI₂), followed by the
 81 conversion of the precursor to perovskite by infiltrating a
 82 reaction solution, leading to the so-called embedment C-
 83 PSCs.^{21,22} In paintable C-PSCs, the carbon electrode is directly
 84 deposited onto the perovskite layer, or the hole-transporting
 85 layer (HTL), or the electron-transporting layer (ETL)
 86 depending on the device configuration (i.e., CTL-free devices,
 87 n-i-p and p-i-n configurations, respectively).^{23,24} The main
 88 acclaimed advantages of C-CEs are as follows:^{16,17,25} (1) low
 89 cost, which, however, strongly depends on the type of the
 90 carbon materials. The hole-extraction properties of C-CEs can
 91 also eliminate the use of (expensive) HTLs required for noble
 92 metal-based CEs;^{23,25,26} (2) chemical inertness to halide ions,
 93 which eliminates the corrosion of metallic CEs;⁹ and (3)
 94 hydrophobic characteristics, which intrinsically limit the intake
 95 of moisture.²⁷ These features are considered a breakthrough
 96 for the reduction of the LCOE of the current PSC
 97 technology.²⁸ Unfortunately, the PCEs of C-PSCs still lag
 98 behind those of the most efficient Au-based PSCs.¹⁷
 99 Furthermore, several C-PSCs with PCEs higher than 15%
 100 are often based on (doped) carbon nanotubes, which have
 101 been used as a hydrophobic additive in the perovskite layer,²⁹
 102 highly conductive and hole-extracting CE materials,^{30,31} and

interlayers electrically connecting the perovskite to the
 CEs.^{32,33} Regrettably, the cost of solar-grade carbon nanotubes,
 including single-/double-walled ones, can be even superior to
 the one of noble metals.³⁴ The highest PCE of 19.2% has been
 reached by “paintable-like” C-PSCs,³⁵ in which the C-CE was
 realized through the hot-press transfer method.^{35–37} Although
 this method is compatible with high-throughput roll-to-roll
 manufacturing and/or laminating processes,^{35,36,38} its precise
 control over a large area has just been reported in 1 cm² PSCs
 using a conductive (sheet resistance $R_{\text{sheet}} < 1 \Omega \text{ sq}^{-1}$) graphite
 paper or aluminum foil as the substrate for the C-CEs (PCE =
 17.4 and 15.41%).³⁹ Meanwhile, perovskite solar modules
 (PSMs) based on hot-press transferred C-CEs have not been
 tested yet. On the contrary, printed C-PSCs have been
 upscaled into large-area configurations and PSMs^{20,40–43} and
 even into solar farms (up to 7 m² area).^{40,42} In these
 circumstances, both screen printing⁴⁰ and mechanical scrib-
 ing⁴⁴ have been proposed as methods to pattern the C-CEs for
 the serial interconnection of the cells in prototypical PSMs.
 Meanwhile, the use of advanced HTL, such as poly(3-
 hexylthiophene-2,5-diyl) (P3HT)/graphene composite, en-
 abled paintable C-PSCs to reach a record-high PCE of
 18.2% (certified value up to 17.8%).⁴⁶ Recent reviews on C-
 PSCs summarized the origin of their performance loss
 compared to state-of-the-art devices,^{16,47} which is consensually
 attributed to the insufficient charge-selective properties of the
 C-CEs as well as to charge recombination processes at the back
 interface (i.e., perovskite/CE or CTL/CE).¹⁷ The engineering
 of perovskite, CE, and interlayer represents common strategies
 to mitigate the current C-PSC limitations.¹⁷ Nevertheless,
 paintable C-PSCs based on low-temperature-processed CEs
 are currently considered convenient configurations to close the
 PCE gap between C-PSC and noble-metal ones.¹⁷ In
 particular, the knowledge used for the fabrication of the
 state-of-the-art PSCs is directly transferable into such C-
 PSCs.¹⁷ In fact, low-temperature-processed C-CEs (1) can be
 easily integrated with established effective CTLs. Meanwhile,
 they are (2) compatible with large perovskite crystals, which
 are not constrained by the pore size of mesoporous C-CEs in
 C-PSCs; (3) applicable to flexible configurations, enabling low-

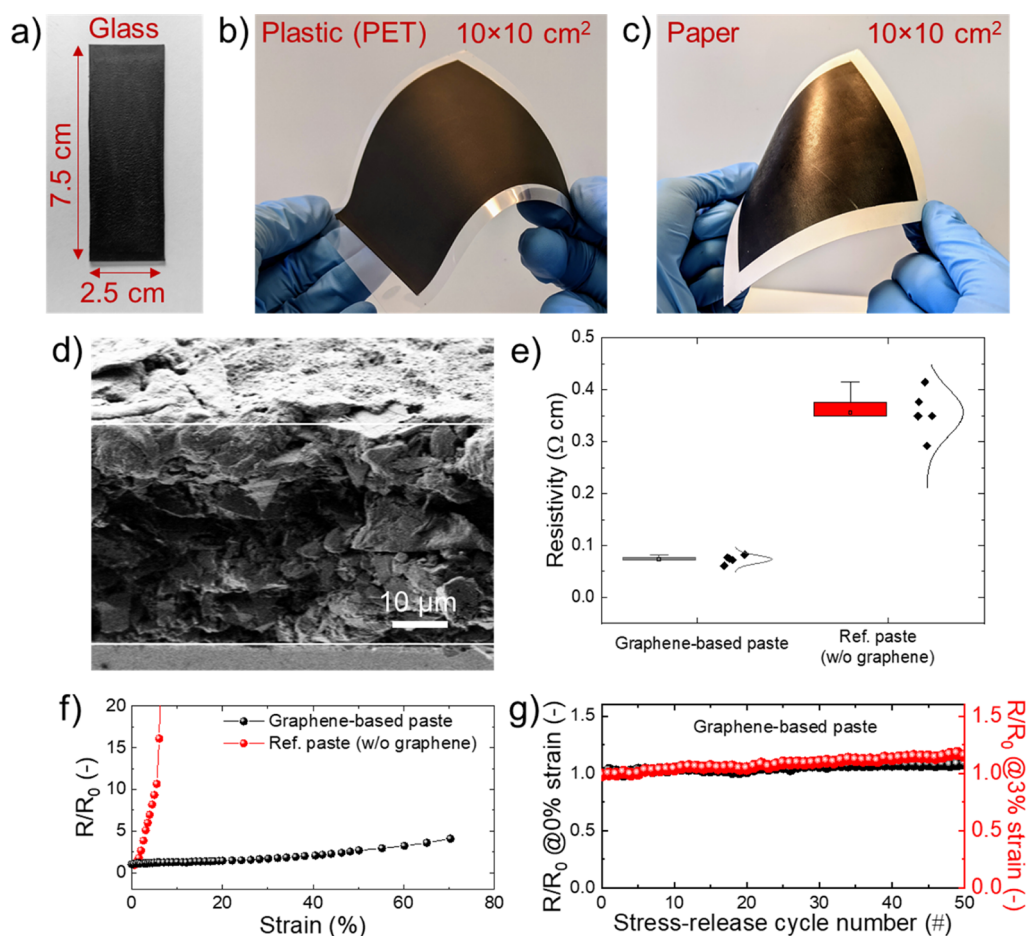


Figure 2. Photographs of graphene-based carbon paste deposited onto different substrates: (a) glass; (b) PET; and (c) paper. (d) Cross-sectional SEM image of a film obtained by depositing the graphene-based carbon paste (thickness *ca.* 40 μm). (e) Statistics for the electrical resistivity of the films obtained by depositing graphene-based pastes and reference pastes (w/o graphene). (f) Resistance (R) of the films obtained by depositing graphene-based pastes and reference pastes (w/o graphene) normalized on the initial value (strain = 0%) (R_0) as a function of the strain and (g) the number of S–R cycles at a tensile strain of 3%.

143 cost, roll-to-roll manufacturing processes; and (4) highly
144 scalable since their short sintering optimally matches with the
145 highest production rate reported so far for the underlying PSC
146 structures (in the order of 0.1 $\text{m}^2 \text{min}^{-1}$).^{48,49}

147 By rationalizing the technological status of C-PSCs, we
148 report an affordable and facile fabrication of paintable C-PSCs
149 based on C-CEs directly printed atop of efficient prototypical
150 PSC configurations (Figure 1). Small-area 0.09 cm^2 and large-
151 area 1 cm^2 Au-based reference devices and paintable C-PSCs
152 were fabricated either in mesoscopic or low-temperature-
153 processed planar configurations (Figure 1a–d). For the
154 mesoporous devices, graphene-doped TiO_2 ETLs were used
155 to improve the performance of mesoscopic C-PSCs based on
156 pristine ETLs, in agreement with our previous works.^{50–52} The
157 C-CEs were realized by depositing commercially available
158 pastes based on thermoplastic binders and a high vapor
159 pressure alcoholic solvent [i.e., isopropyl alcohol (IPA)], which
160 does not damage the underlying layers. Despite its simplicity,
161 our approach enables small-area (0.09 cm^2) mesoscopic C-
162 PSCs to achieve a maximum PCE of 15.81%. To prove their
163 versatility and scalability, the proposed C-CEs were applied to
164 large-area (1 cm^2) mesoscopic devices and low-temperature-
165 processed planar n–i–p devices based on SnO_2 ETL, reaching
166 PCEs of 13.85 and 14.06%, respectively. Remarkably, the PCEs
167 of our all-printed large-area C-PSC are superior to the record-

high values reported in the literature for large-area C-
PSCs^{20,39,42,53–58} in the absence of back-contact metalliza-
tion^{39,53,59} and additional stacked conductive components
(e.g., graphite and ITO).^{39,60}

Based on these results, we realized a proof-of-concept
metallized miniwafer-like area C-PSC (substrate area = 6.25
 cm^2 , aperture area = 4.00 cm^2) (Figure 1e), reaching a PCE on
active area of 13.86% and a geometric fill factor (FF_{geom} , also
called aperture ratio) of $\sim 87.3\%$, corresponding to a record-
high PCE on aperture area of 12.1%. In this regard, we discuss
that monolithic wafer-like area PSCs can represent all solution-
processed configurations, which are more reliable than
prototypical serial PSM configurations in developing practical
perovskite solar plants since (1) they mitigate hysteresis-
induced performance loss⁶¹ and hot-spot-induced irreversible
material (perovskite and CTL) damage caused by reverse
biases⁶² and (2) they have the potential to maximize the
 FF_{geom} using high-resolution metallization processes widely
established in PV technologies besides the PSCs.

RESULTS AND DISCUSSION

Carbon-Based Counter Electrodes. The C-CEs investi-
gated here were produced by printing commercial low-
temperature-processed carbon pastes supplied by BeDimen-
sional S.p.A.⁶³ The pastes are given by a mixture of the 191

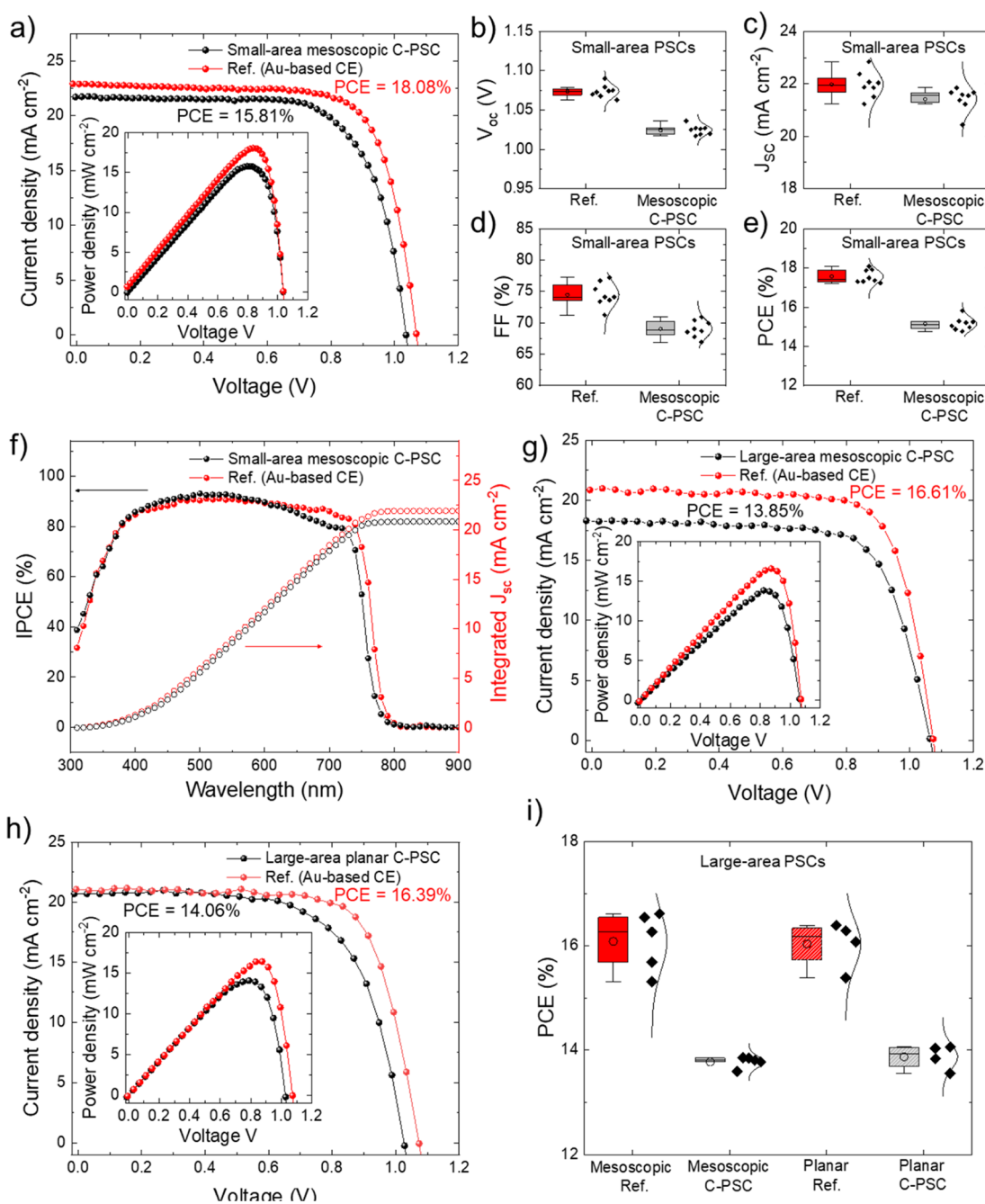


Figure 3. (a) J - V curves (reverse voltage scan) measured for the most efficient small-area (active area = 0.09 cm^2) mesoscopic C-PSC using graphene-doped ETLs and Au-based reference. The inset panel shows power density vs voltage plots measured for the same devices; (b–d) statistics of the PV figure of merit measured in the reverse voltage scan mode for the small-area (active area = 0.09 cm^2) mesoscopic C-PSCs using graphene-doped ETLs and Au-based references: V_{oc} (b), J_{sc} (c), FF (d), and PCE (e). (f) IPCE spectra for representative small-area (active area = 0.09 cm^2) mesoscopic C-PSC using graphene-doped ETLs and Au-based reference. (g) J - V curves (reverse voltage scan) measured for the most efficient large-area (active area = 1 cm^2) mesoscopic C-PSC using graphene-doped ETLs and Au-based reference. The inset panel shows power density vs voltage plots measured for the same devices. (h) J - V curves (reverse voltage scan) measured for the most efficient large-area (active area = 1 cm^2) low-temperature-processed planar C-PSC and Au-based reference. The inset panel shows power density vs voltage plots measured for the same devices. (i) Statistics of the PCE measured in the reverse scan mode for the large-area (1 cm^2) mesoscopic and planar C-PSCs and Au-based references.

192 following composition: (1) carbon black and single/few layer
 193 graphene flakes as the electrically conductive component; (2)
 194 thermoplastic polymers as the binder; and (3) high vapor
 195 pressure alcohols, including IPA, as the solvent. The graphene
 196 flakes are produced through the evaporation and freeze-drying
 197 of a dispersion of flakes produced by the scalable wet-jet
 198 milling (WJM) exfoliation of graphite, as disclosed in patent

nr. WO2017/089987A1.⁶⁴ Briefly, the WJM exfoliation 199
 process exploits a high pressure (between 180 and 250 200
 MPa) to force the passage of the solvent/graphite mixture 201
 through perforated disks, with adjustable hole diameters (0.3– 202
 0.1 mm, named nozzle), generating shear forces which exfoliate 203
 the graphite.^{65,66} Such an exfoliation method provides a 204
 production rate of graphene flakes of $\sim 0.4 \text{ g min}^{-1}$ (on a single 205

WJM apparatus) and an exfoliation yield of 100%.^{65,66} These features make the WJM-produced graphene flakes affordable for massive applications (contrary to other highly conductive graphitic materials, e.g., carbon nanotubes).⁶⁷ Differently from other chemical exfoliation and chemical/thermal reduction methods used for the production of graphene derivatives (e.g., reduced graphene oxides),^{68,69} the WJM exfoliation process preserves the chemical purity of the starting graphite. Meanwhile, it avoids the formation of functional groups and structural defects in the graphene basal planes,^{65,66} which deteriorate the ideal graphene properties, including electrical conductivity.^{70,71} By adjusting the concentration of their solid content, the pastes can be deposited on both rigid (e.g., glass) and flexible (e.g., polyethylene terephthalate, PET, and paper) substrates using common printing techniques, including doctor-blading and spray coating (Figure 2a–c) as well as spin coating (as shown hereafter). For all the cases, the deposition temperature of the paste can be inferior to 100 °C and can be even at ambient temperature. Depending on the temperature, the curing time for tens of micrometers thick films ranges from seconds/tens of seconds (for temperature around 100 °C) to tens of minutes (for ambient temperature). Figure 2d shows a cross-sectional scanning electron microscopy (SEM) image of a ~40 μm thick film obtained by depositing the graphene-based carbon paste by doctor blading (films cured at 40 °C for ca. 5 min). The presence of graphene flakes is distinguishable within the binder matrix. As shown in Figure 2e, the use of graphene flakes enables the C-CEs to reach a resistivity as low as $0.07 \pm 0.01 \Omega \text{ cm}$, corresponding to an R_{sheet} of $\sim 17 \Omega \text{ sq}^{-1}$ for a thickness of 40 μm. Such an R_{sheet} is similar or inferior to the values reported for common transparent conductive oxide (TCO)-based CE and C-CEs.^{72,73} Remarkably, a reference paste without graphene shows a 5-fold increase of the resistivity compared to the graphene-based paste (resistivity = $0.35 \div 0.06 \Omega \text{ cm}$). Thus, graphene-based C-CEs are expected to alleviate the drawback (e.g., low FF) related to the high series resistance of current collectors in large-area solar cells.^{74,75} In addition, graphene-based films show optimal mechanical properties, which may be beneficial to tolerate thermomechanical stresses associated with natural weathering (day/night cycles, as simulated by the IEC 61215:2016 damp heat test⁷⁶) and metallization–encapsulation processes.⁷⁸ As shown in Figure 2f, they withstand tensile strains before neat fracture >70% (fracture strain of PET), while a reference film without graphene breaks to a tensile strain lower than 10%. Moreover, the graphene-based films optimally retain their electrical conductivity over 50 stretch–release (S–R) cycles at a tensile strain of 3%, while the films without graphene did not withstand the first release after stretching (Figure 2g).

Device Fabrication and Characterization. To assess the effectiveness of our (graphene-based) C-CEs, small-area (0.09 cm²) and large-area (1 cm²) Au-based reference devices and paintable C-PSCs were fabricated either in mesoscopic or low-temperature-processed planar configurations (Figure 1a–d). First, prototypical mesoscopic n–i–p devices were produced with the following structure: glass/fluorine tin oxide (FTO)/cTiO₂/mTiO₂/perovskite/spiro-OMeTAD/C-CE (or Au-based CE) (Figure 1a,b), in which the perovskite is the triple cation Cs_{0.05}(FA_{0.85}MA_{0.15})_{0.95}Pb(I_{0.85}Br_{0.15})₃.^{52,79} Although spiro-OMeTAD is an expensive HTL with stability issues, it was used in this work to provide proof-of-concept C-PSCs that can be prospectively modified using the most advanced, stable,

and viable HTLs established in recent literature studies.^{80,81} In a second device version, both cTiO₂ and mTiO₂ were doped with graphene flakes (ETLs named cTiO₂ + graphene and mTiO₂ + graphene, respectively) (Figure 1c). To dope cTiO₂ and mTiO₂, the cTiO₂ precursor solution and the mTiO₂ paste were mixed with the commercial WJM-produced graphene dispersion in ethanol: water (see additional details in the Supporting Information). We have previously shown that graphene doping improves the electrical conductivity of cTiO₂/mTiO₂, thus accelerating the electron extraction toward the front CE.^{50–52} Furthermore, graphene flakes regulate the perovskite crystal growth over mesoscopic scaffolds, including m-TiO₂, increasing the reproducibility of the active layer deposition.⁸² Meanwhile, graphene flakes act as stabilizers for the perovskite, slowing down charge thermalization processes, potentially enabling advanced hot-carrier extraction- and collection-exploiting device concepts.⁸³ The photographs of representative small-area and large-area mesoscopic devices using graphene-doped ETLs are reported in Figure S1. Apart from TiO₂-based ETLs, SnO₂-based ETLs were also produced through spin coating for large-area 1 cm² low-temperature-processed PSCs (Figure 1d). The C-CEs (graphene-based carbon paste) were deposited by spin coating directly onto spiro-OMeTAD. As shown in our previous works on PSCs and PSMs, by depositing two-dimensional MoS₂ inks as buffer layers between spiro-OMeTAD and Au CEs,^{52,84,85} alcoholic solvents can preserve the integrity of the underlying perovskite/spiro-OMeTAD structure. The protocols used for the material preparation and device manufacturing follow those reported in previous literature⁸⁶ and are described in detail in the Supporting Information. In addition to 1 cm² area PSCs, metallized miniwafer-like area mesoscopic C-PSCs were produced on 6.76 cm² substrates (see additional details of the layout in the Supporting Information). Both front electrode (FTO) and back C-CE were metallized by three Au stripes, as depicted in Figure 1e, to avoid series resistance losses. Such a prototype architecture aims to mimic the ones used for wafer-area solar cells,⁸⁷ including the massively commercialized Si-based SCs.⁸⁸ Hereafter, the advantages of monolithic wafer-like area PSCs compared with prototypical (mini)module configurations (i.e., serially connected solar cells reaching a total active area approaching to the wafer scale^{40,41,52}) will be thoroughly discussed.

Figure 3a reports the current–voltage (J – V) curve (reverse voltage scan) measured for the most efficient small-area (active area = 0.09 cm²) mesoscopic C-PSC using graphene-doped ETLs under 1 sun illumination in comparison with the J – V curves measured for the best reference cell using Au-based CEs. The PCE of the mesoscopic C-PSCs is as high as 15.81%, representing a 12.5% decrease relatively to the Au-based reference (PCE = 18.08%). Remarkably, our C-PSCs exhibit a high V_{oc} of 1.04 V and an FF of 70.44%, which is not easily reported for paintable C-PSCs in the absence of back-contact metallization^{39,53,59} or additional stacked conductive components (e.g., graphite and ITO).^{39,60} The inset of Figure 3a shows the power density versus voltage plots of the champion devices, indicating maximum power densities of 15.86 and 18.10 mW cm^{−2} for mesoscopic C-PSCs and Au-based reference, respectively. Figure 3b–e shows the statistics of the PV figures of merit [namely, open-circuit voltage (V_{oc}), short-circuit current density (J_{sc}), FF, and PCE] for the investigated small-area mesoscopic PSCs, as extracted by their J – V curves in the reverse voltage scan mode. Clearly, the 331

mesoscopic C-PSCs show reproducible results over various cells, resulting in an average PCE of 15.15%. The statistics of the PV figures of merit extracted from $J-V$ curves acquired in the forward voltage scan mode are reported in Figure S2, indicating a similar hysteresis behavior for the C-PSCs and Au-based references (average PCEs of $16.02 \pm 0.56\%$ and $13.77 \pm 0.31\%$, respectively). The characterization of the C-PSCs obtained with undoped ETLs is reported in the Supporting Information (Figure S3). The average PCE of the device with undoped ETLs decreases by $\sim 8.6\%$ compared to devices with graphene-doped ETLs, confirming the beneficial role of the graphene doping for the ETLs in mesoscopic devices.^{50,52,82,89} Figure 3f shows the incident photon-to-current efficiency (IPCE) spectra measured for representative small-area mesoscopic C-PSCs and the Au-based reference, with PCEs of 15.81 (champion device) and 17.36%, respectively. The integrated J_{sc} values match the ones extrapolated from the $J-V$ curves measured for the most efficient devices. The IPCE data reveal that major IPCE losses in the C-PSCs compared to the Au-based reference occur in the spectral region between 630 and 800 nm. Even though we do not have a clear explanation of the IPCE loss in our C-PSCs, we speculate that the deposition of the carbon paste may affect the original devices' interfaces, causing a recombination of the charges photo-generated by the light with the lowest energies. Although the solvent used for the graphene-based carbon paste, namely, IPA, has been proved to be compatible with the perovskite in our previous works,^{52,84} it may still have some influence on the quality of the spiro-OMeTAD HTL and related interfaces. In this context, the combination of our graphene-based carbon paste technology with advanced HTLs alternative to spiro-OMeTAD is promising to further boost the PV performances obtained in our work while decreasing the overall device costs. Figure 3g reports the $J-V$ curves (reverse voltage scan) measured for the champion large-area (active area = 1 cm^2) mesoscopic C-PSCs (C-CE produced by spin coating the graphene-based carbon paste) and the corresponding Au-based reference. The cells achieved PCEs of 13.85 and 16.61%, respectively. In addition, mesoscopic C-PSCs were also produced by depositing the graphene-based C-CEs through the doctor blading method, reaching a maximum PCE as high as 12.33% (Figure S4, Table S1). Similar C-PSC architectures with C-CEs produced by depositing a commercially available carbon paste, instead of our graphene-based carbon paste, reached a maximum PCE of 8.7% (see additional details in Supporting Information, Figure S5), which was significantly inferior to the PCEs reached by our device. The superior PV performances obtained using the graphene-based pastes compared to those achieved using other commercial carbon pastes may be related to the different solvents used in paste formulation (IPA for the graphene-based paste investigated in our work; 2-(2-ethoxyethoxy)ethyl acetate, 2-methylnaphthalene, and pentylbenzene for the commercial paste used for comparison), as well as to the optimal mechanical and electrical properties provided by the graphene flakes to the C-CEs.

In addition, HTL-free C-PSCs were also produced by eliminating the spiro-OMeTAD HTL from the device architecture. The HTL-free prototypes reached a PCE of 9.62% (Figure S6), which is promising for the realization of low-cost PSCs. The stability of the small-area cells was evaluated through ISOS-D-1 (shelf life at ambient temperature and relative humidity) and ISOS-D-2 (shelf life at 85°C and

ambient relative humidity) protocols⁹⁰ on unencapsulated devices (Figure S7), as described in ref 91. Under the ISOS-D-1 test, the C-PSCs and Au-based references exhibited a similar stability. In particular, all the devices retained more than 90% of their initial PCE (average normalized PCE after 360 h > 93%). Under the ISOS-D-2 test, the Au-based references exhibited a T_{80} lifetime (here defined as the time spans in which the average normalized PCE of the devices is equal to 80%) of 51.9 h, while the C-PSC reached a T_{80} of 173.1 h, indicating a stability improvement compared to the Au-based reference. Nevertheless, the stability data of the unencapsulated devices indicated that the C-CEs improve the overall stability of the devices compared to the case of Au-based CEs. In this context, the recent development of advanced encapsulants is promising for the PSC technology¹³ and can be prospectively applied to our C-PSCs. The replacement of spiro-OMeTAD with more stable HTL may also be beneficial to further improve the stability of our C-PSCs. To further extend the applicability of our C-CEs while exploiting their full potential, large-area (1 cm^2) low-temperature-processed planar C-PSCs were fabricated using SnO_2 ETLs. Figure 3h shows the $J-V$ curve (reverse voltage scan) of the champion large-area planar C-PSC and the corresponding Au-based reference. Remarkably, the planar C-PSCs reached a PCE as high as 14.06%, corresponding to an only 14.2% decrease relatively to the Au-based reference (PCE = 16.36%). Figure 3i summarizes the statistics for the PCEs measured for the large mesoscopic and planar devices. The statistics for the other figures of merit for the large-area devices are reported in the Supporting Information (Figure S8).

The PCEs achieved by our 1 cm^2 area C-PSCs are among the highest reported values for large-area C-PSCs^{20,29,42,53–58} in the absence of back-contact metallization^{39,53,59} or additional stacked conductive components (e.g., graphite and ITO)^{39,60} or vacuum thermally evaporated protective metallic layers (e.g., Cr)⁵⁸ (Figure 4 and Table S2). The results demonstrated here are ascribed to both the high conductivity of graphene-based C-CE (see Figure 1) and the compatibility of the low-temperature processable and alcoholic solvent-based carbon pastes with the underlying PSC layers.

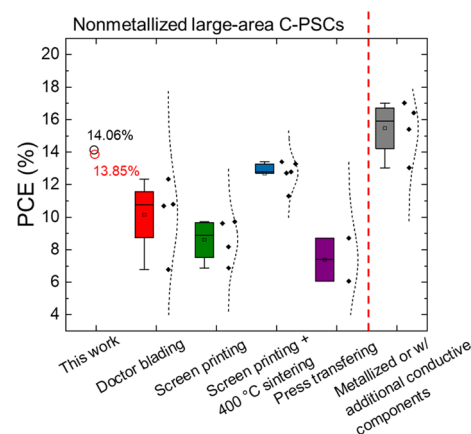


Figure 4. Statistics of PCEs of large-area C-PSCs reported in relevant literature studies.^{20,29,39,42,53–60,92–96} The C-PSCs are classified according to the C-CE deposition/application method. The last C-PSC class refers to C-PSCs with metallized C-CE (i.e., Cu grid⁵³ or Al foil³⁹) or additional conductive components stacked on C-CE (i.e., graphite paper³⁹ or ITO⁶⁰).

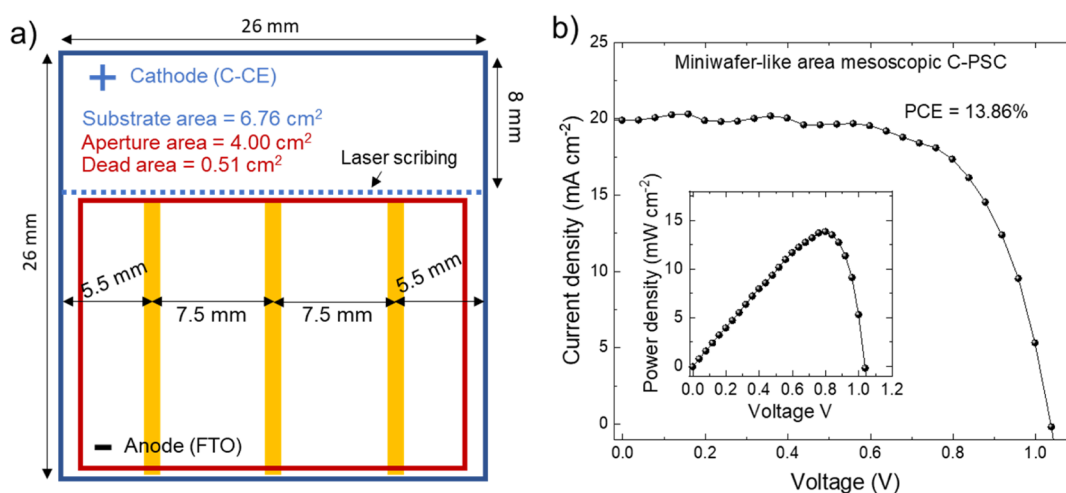


Figure 5. (a) Layout of the miniwafer-like area mesoscopic C-PSCs using graphene-doped ETLs, showing the front contact (i.e., FTO) Au-based metallization. A nearly specular Au-based metallization layout was used for the C-CE, as shown by the photograph of the device from its back contact (Figure S8). The aperture area corresponds to the region delimited by the red line. (c) J - V curve (reverse voltage scan) measured for the miniwafer-like area C-PSC (aperture area = 4.00 cm², dead area = 0.51 cm²). The inset panel shows the power density vs voltage plot measured for the same device, while the right one is a photograph of the miniwafer-like area C-PSC.

After assessing the reproducible fabrication of large-area C-PSCs, metallized miniwafer-like area C-PSCs were produced on 6.76 cm² substrates (aperture area = 4.00 cm²) according to the layout shown in Figure 5a for the front contact. Figure S9 shows the photographs of the device from its back contact (i.e., the C-CE). Both the front electrode (FTO) and back C-CE were metallized by three thermally evaporated, thin (100 nm) Au stripes (width = 1 mm) to avoid series resistance losses with upscaling of the cell area.^{75,97} In fact, electrode collection paths longer than 1 cm cause significant power loss or FF reduction due to the intrinsic resistance of the current collectors (e.g., in the order of 10 Ω sq⁻¹ for prototypical TCOs, including FTO).⁹⁸ We are aware that the accurate design of the grid architecture needs to consider several factors, for example:^{97,98} (1) the loss of the active area available for illumination; (2) the physical thickness (height) of the grid lines to achieve the lowest possible grid resistances while maintaining compatibility with the thin-film junction forming the solar cell to avoid shorting defects; and (3) the spacing and arrangement of the grid lines to reduce the carrier collection path length to less than the critical length defined by the sheet resistance of the current collectors. Despite the complexity of the grid design, it was not our goal to optimize the layout of the proposed metallized large-area device, this task being more convenient to be implemented on devices even larger than the ones investigated by this work. Nevertheless, our prototype architecture aimed to prove the possibility to use metallic grids typically applied to wafer-area solar cells (e.g., Si solar cells)^{87,88} to decrease the series resistance associated with both front and back current collectors. To accomplish this objective, we opted for a mesoscopic configuration to enter in the so-called “thick-junction regime”.^{97,99} In fact, the ETL layers (graphene-doped cTiO₂ and graphene-doped mTiO₂) that cover the Au-metallized FTO approach the μm scale thickness so that they avoid possible electrical shorts raised in the presence of the nonhomogeneous perovskite active layer (which is still plausible over large areas, i.e., ≫ 1 cm²). Since our device prototype combines solution-processed C-CE, the replacement of thermally evaporated Au stripes with solution-processed metal grids may easily enable solution-processed

wafer-like area PSCs.⁹⁹ Figure 5b shows the J - V curve (reverse voltage scan) measured with our metallized miniwafer-like area mesoscopic C-PSC, which achieved a PCE of 13.86 [value calculated on the active area, i.e., (aperture area—dead area)], which is comparable to the PCE measured for the champion 1 cm² area mesoscopic PSCs (PCE = 13.85%). This means that the device layout effectively avoids power losses originated by the electrical resistance of current collectors (FTO and C-CE) and the metallization is compatible with the upscaling of the device area. These results should spur research studies toward the realization of viable wafer-like area (i.e., 5/6 inches square) (C-)PSCs by means of solution-processed techniques, replacing the current (mini)module configurations based on the serial connection of perovskite subcells.^{41,43,100} The next section reports some technical considerations which justify the importance, according to our point of view, of moving from the serial PSM configuration to wafer-like area PSCs.

Serial Perovskite Solar Minimodules or Monolithic Wafer-like Area Devices? Technical Considerations and Perspectives. Serial PSM configurations have been widely established to intrinsically avoid power losses originated by the electrical resistance of large-area transparent electrodes without requiring any additional metallization of the transparent electrodes.^{41,43,100} It is noteworthy that serial module configurations have also been established in other thin-film PV devices,¹⁰¹ where laser scribing processes can be used to achieve a high FF_{geom}^{102,103} defined as the ratio between the active area and the aperture area (active area + dead area) of the device. In fact, the serial module configurations keep the current as small as that of each subcell while increasing the output voltage up to the sum of voltage of each subcell. However, two drawbacks arise for such architecture:¹⁰⁴ (1) it is highly sensitive to the cell electrical current mismatches,¹⁰⁵ which are introduced by layer inhomogeneities as well as shadows on the device area;¹⁰⁶ (2) the patterning processes (e.g., laser scribing) established on Au-based CEs to realize serially connected subcells while minimizing the size of the “dead areas”¹⁰⁷ cannot be directly applied to micrometers thick C-CEs.⁴⁴ More in detail, shaded solar cells produce lower electrical current than the unshaded ones and force the in 514

515 series-connected unshaded cells to deliver a low electrical
516 current compared to their nominal ones.^{105,106} Furthermore,
517 the shaded cells are forced to operate in reverse bias by the
518 other cells in the string to conduct their higher electric current
519 and eventually act as a load dissipating the power that is
520 generated by the unshaded cells and locally heating up. This
521 effect can result in the so-called “hot-spot”-induced malfunc-
522 tion,¹⁰⁸ irreversibly damaging the entire solar module. These
523 degrading effects are well-known for commercially available PV
524 technologies¹⁰⁹ but are rarely discussed for PSCs,^{61,62,110} in
525 which “hot-spot” effects can be even more deleterious because
526 of the limited thermal stability of perovskite (as well as several
527 CTLs) at temperatures higher than 100/120 °C.⁷ In principle,
528 bypass diodes (BPDs) may be used to bypass the irradiated
529 solar cells^{111,112} This approach is commonly used in
530 commercial Si solar modules, in which a BPD is connected
531 in parallel to strings of 15–24 cells connected in series to
532 prevent shaded cells from reaching the junction breakdown.¹¹²
533 However, we expect two crucial complications on the use of
534 BPDs for the case of perovskite solar minimodules. (1) The
535 current generated in the unshaded subcells must be trans-
536 ported toward the PBDs parallel to the shaded cells through
537 the current collectors (e.g., in an n–i–p configuration, TCO
538 from the front side, and Au or C-CE from the back side),
539 which must therefore display low electrical resistance values.
540 Unfortunately, the TCO current collectors have resistivity in
541 the order of 10 Ω sq⁻¹, which is insufficient to collect the
542 current toward the BPDs, causing unreliable reverse-bias
543 protection. (2) During the activation of a BPD in the presence
544 of one shaded cell, the maximum reverse voltage in a single
545 shaded cell ($|V_{\text{REV}}|_{\text{max}}$) is determined by the number of cells in
546 the string, their V_{oc} , and the forward voltage (V_{F}) of the
547 BPD¹¹³

$$|V_{\text{rev}}|_{\text{max}} \leq \left(\sum_{i=1}^{n-1} V_{\text{oc},i} + V_{\text{F}} \right)$$

548 where n is the number of the cells in the string. Importantly, |
549 $V_{\text{REV}}|_{\text{max}}$ must be inferior to the breakdown voltage (V_{BD}) of
550 the cell in order to avoid the junction breakdown of the cell.¹¹³
551 For the case of Si solar cells, V_{BD} is typically ≥ 12 V, V_{oc} is
552 typically ≤ 0.75 V, and $n = 24$, safely avoiding the chance of
553 reaching V_{BD} by a single cell. Unfortunately, V_{BD} for PSCs is
554 typically < 5 V,^{61,62} while V_{oc} easily reaches values above 1 V
555 (as shown in this work). Even more, the junction breakdown in
556 the PSCs is triggered by the accumulation of ionic defects at
557 the interfaces, which brings irreversible degradation and
558 hysteresis phenomena, degrading both the short- and long-
559 term PV performance of the entire minimodule.⁶¹ Based on
560 these considerations, the low V_{BD} of the PSCs would require a
561 large amount of BPDs to prevent damages and such an amount
562 of BPDs would inevitably increase the system costs of
563 perovskite PVs to an uncompetitive value.¹¹² In this context,
564 wafer-like area C-PSCs could intrinsically overcome the above
565 limits of perovskite minimodule serial configuration while
566 providing a solution-processed cell fabrication (except for the
567 starting TCO substrate) without recurring to expensive high-
568 resolution film patterning processes (e.g., laser scribing),¹¹⁴
569 whose implementation is still unreported on tens of micro-
570 meters thick C-CEs. To the best of our knowledge, just screen
571 printing and one example of mechanical scribing⁴⁴ are reported
572 for C-CEs, resulting in FF_{geom} lower than 80% (more
573 commonly $\leq 70\%$).⁴⁴ In our basic layout, by excluding the

area left for the top and bottom contacts, the FF_{geom} is $\sim 87.3\%$,⁵⁷⁴
which is already comparable to the highest values reported for
575 laser-scribed PSMs using Au as the CE^{114,115} and superior to
576 the FF_{geom} reported for carbon PSMs.^{20,40–42,44,53,55,56,116}
577 Table S3 reports a summary of the PCE and FF_{geom} values
578 obtained for PSMs based on C-PSCs connected in series, as
579 reported in literature studies.^{20,40–42,44,53,55,56} Clearly, our
580 technology, although the active and aperture areas are still
581 significantly inferior to those reported by serial PSM
582 configurations, has the potential to improve both PCE and
583 FF_{geom} of the current state-of-the-art of wafer-area carbon
584 perovskite PVs. In particular, to the best of our knowledge, our
585 miniwafer-like area device shows a record-high PCE calculated
586 on the aperture area of 12.10%, while previous carbon PSMs
587 reported values lower than 9%.^{20,40–42,44,53,55,56} Last, screen
588 printing of Ag pastes for the metallization of Si solar cells has
589 recently demonstrated printed electrode widths of ~ 20 μm.¹¹⁷
590 Therefore, the metallization of our basic layout through high-
591 resolution screen printing is expected to drastically increase the
592 FF_{geom} achieved by our proof-of-concept devices above 95%,
593 overcoming the record-high FF_{geom} values achieved for Au-
594 based PSMs produced through laser scribing.^{114,115} For the
595 front TCO metallization, innovative current collector concepts
596 based on thick metal grids embedded either in rigid or flexible
597 substrates can preserve the planarity of the metallized front
598 electrode,¹¹⁸ resulting in clear compatibility with the PSC
599 technology, even in the so-called “thin-junction regime” (i.e.,
600 active layer and CTLs with sub-μm thicknesses),^{97,99} including
601 planar (non-mesoscopic) PSC configurations. 602

603 ■ CONCLUSIONS

In summary, we have designed and realized efficient paintable
604 C-PSCs obtained by depositing a commercial low-temper-
605 ature-processed graphene-based carbon paste atop prototypical
606 mesoscopic and planar n–i–p structures. Our small-area (0.09
607 cm²) mesoscopic C-PSCs achieved a maximum PCE of 15.81%
608 while showing an improved thermal stability under the ISOS-
609 D-2 protocol compared to the reference devices based on Au
610 CEs. To prove the versatility and scalability of our technology,
611 the proposed graphene-based CEs were applied to large-area
612 (1 cm²) mesoscopic devices and low-temperature-processed
613 planar n–i–p devices, reaching PCEs of 13.85 and 14.06%,
614 respectively. To the best of our knowledge, these PCE values
615 are among the highest reported for large-area C-PSCs in the
616 absence of back-contact metallization or additional stacked
617 conductive components or a thermally evaporated barrier layer
618 between the CTL and the C-CE (strategies commonly used for
619 the record-high efficiency of C-PSCs). Based on these results,
620 we realized a proof-of-concept metallized miniwafer-like area
621 C-PSCs (substrate area = 6.76 cm², aperture area = 4.00 cm²),
622 reaching a PCE on active area of 13.86% and a PCE on
623 aperture area of 12.10%. The obtained results prove the
624 metallization compatibility with our C-PSCs. Last, we
625 discussed how monolithic wafer-like area PSCs can represent
626 configurations more reliably than the prototypical serial
627 perovskite solar (mini)modules based on the serial connection
628 of subcells. In particular, wafer-like area C-PSCs have the
629 potential to intrinsically mitigate the reverse-bias effects that
630 cause hysteresis-induced performance loss and hot-spot-
631 induced irreversible material damage in serial perovskite solar
632 (mini)module configurations. Meanwhile, their compatibility
633 with metallization processes is promising for the realization of
634 all solution-processed wafer-like area C-PSCs with a high 635

636 FF_{geom} (>90%), without recurring to expensive and poorly
637 reproducible laser scribing processes.

638 ■ ASSOCIATED CONTENT

639 ■ Supporting Information

640 The Supporting Information is available free of charge at
641 <https://pubs.acs.org/doi/10.1021/acsami.1c02626>.

642 Methods; supplementary PV characterization of small-
643 area PSCs; photographs of small-area and large-area Au-
644 based PSCs and C-PSCs; ISOS-D-1 and ISOS-D-2
645 stability tests on small-area PSCs; statistics for the PV
646 figure of merit for large-area graphene-engineered
647 mesoscopic and planar C-PSCs and Au-based refer-
648 ences; and comparison between our device perform-
649 ances and those reported in the literature (PDF)

650 ■ AUTHOR INFORMATION

651 Corresponding Authors

652 **Aldo Di Carlo** – CHOSE—Centre for Hybrid and Organic
653 Solar Energy, University of Rome Tor Vergata, 00133 Rome,
654 Italy; ISM-CNR, Istituto di Struttura della Materia,
655 Consiglio Nazionale delle Ricerche, 00133 Rome, Italy;
656 orcid.org/0000-0001-6828-2380; Email: aldo.dicarlo@uniroma2.it

658 **Sebastiano Bellani** – BeDimensional S.p.A., 16163 Genova,
659 Italy; Email: s.bellani@bedimensional.it

660 **Francesco Bonaccorso** – BeDimensional S.p.A., 16163
661 Genova, Italy; Graphene Labs, Istituto Italiano di Tecnologia,
662 16163 Genova, Italy; orcid.org/0000-0001-7238-9420;
663 Email: f.bonaccorso@bedimensional.it

664 Authors

665 **Paolo Mariani** – CHOSE—Centre for Hybrid and Organic
666 Solar Energy, University of Rome Tor Vergata, 00133 Rome,
667 Italy

668 **Leyla Najafi** – BeDimensional S.p.A., 16163 Genova, Italy

669 **Gabriele Bianca** – Graphene Labs, Istituto Italiano di
670 Tecnologia, 16163 Genova, Italy; Dipartimento di Chimica e
671 Chimica Industriale, Università degli Studi di Genova, 16146
672 Genoa, Italy

673 **Marilena Isabella Zappia** – BeDimensional S.p.A., 16163
674 Genova, Italy; Department of Physics, University of Calabria,
675 87036 Rende, Cosenza, Italy

676 **Luca Gabatell** – BeDimensional S.p.A., 16163 Genova, Italy

677 **Antonio Agresti** – CHOSE—Centre for Hybrid and Organic
678 Solar Energy, University of Rome Tor Vergata, 00133 Rome,
679 Italy

680 **Sara Pescetelli** – CHOSE—Centre for Hybrid and Organic
681 Solar Energy, University of Rome Tor Vergata, 00133 Rome,
682 Italy

683 Complete contact information is available at:

684 <https://pubs.acs.org/doi/10.1021/acsami.1c02626>

685 Author Contributions

686 The manuscript was written through contributions of all
687 authors. All authors have given approval to the final version of
688 the manuscript.

689 Notes

690 The authors declare no competing financial interest.

691 ■ ACKNOWLEDGMENTS

This project has received funding from the European Union's
692 Horizon 2020 research and innovation program under grant
693 agreement no.785219 and no. 881603-GrapheneCore2 and
694 GrapheneCore3. This project has received funding from
695 European Union's MSCA-ITN ULTIMATE project under
696 grant agreement no. 813036 and from the Italian Ministry of
697 Foreign Affairs and International Cooperation (MAECI)
698 through the Cooperation Project "GINGSENG" (Grant
699 PGR05249) between Italy and China. M.I.Z. received
700 funding from the PON Research and Innovation 2014–2020
701 (CUP H25D18000230006) by the Italian Ministry of
702 University and Research. 703

704 ■ REFERENCES

- 695 (1) Wang, P.; Wu, Y.; Cai, B.; Ma, Q.; Zheng, X.; Zhang, W. H. Solution-Processable Perovskite Solar Cells toward Commercialization: Progress and Challenges. *Adv. Funct. Mater.* **2019**, *29*, 1807661. 706
- 707 (2) NREL. Solar Cell Efficiency Chart. *Cell Efficiency Chart/Photovoltaic Research*; NREL, 2020. 708
- 709 (3) Yoo, J. J.; Seo, G.; Chua, M. R.; Park, T. G.; Lu, Y.; Rotermund, F.; Kim, Y.-K.; Moon, C. S.; Jeon, N. J.; Correa-Baena, J.-P.; Bulović, V.; Shin, S. S.; Bawendi, M. G.; Seo, J. Efficient Perovskite Solar Cells via Improved Carrier Management. *Nature* **2021**, *590*, 587–593. 710
- 711 (4) Jeong, J.; Kim, M.; Seo, J.; Lu, H.; Ahlawat, P.; Mishra, A.; Yang, Y.; Hope, M. A.; Eickemeyer, F. T.; Kim, M.; Yoon, Y. J.; Choi, I. W.; Darwich, B. P.; Choi, S. J.; Jo, Y.; Lee, J. H.; Walker, B.; Zakeeruddin, S. M.; Emsley, L.; Rothlisberger, U.; Hagfeldt, A.; Kim, D. S.; Grätzel, M.; Kim, J. Y. Pseudo-halide anion engineering for α -FAPbI₃ perovskite solar cells. *Nature* **2021**, *592*, 381. 712
- 713 (5) <https://itrpv.vdma.org/> (data accessed on 12 April, 2021). 714
- 715 (6) Jena, A. K.; Kulkarni, A.; Miyasaka, T. Halide Perovskite Photovoltaics: Background, Status, and Future Prospects. *Chem. Rev.* **2019**, *119*, 3036–3103. 716
- 717 (7) Rong, Y.; Hu, Y.; Mei, A.; Tan, H.; Saidaminov, M. I.; Seok, S. I.; McGehee, M. D.; Sargent, E. H.; Han, H. Challenges for Commercializing Perovskite Solar Cells. *Science* **2018**, *361*, No. eaat8235. 718
- 719 (8) Zhou, Y.; Zhao, Y. Chemical Stability and Instability of Inorganic Halide Perovskites. *Energy Environ. Sci.* **2019**, *12*, 1495–1511. 720
- 721 (9) Wang, Q.; Phung, N.; Di Girolamo, D.; Vivo, P.; Abate, A. Enhancement in Lifespan of Halide Perovskite Solar Cells. *Energy Environ. Sci.* **2019**, *12*, 865–886. 722
- 723 (10) Chang, N. L.; Yi Ho-Baillie, A. W.; Basore, P. A.; Young, T. L.; Evans, R.; Egan, R. J. A Manufacturing Cost Estimation Method with Uncertainty Analysis and Its Application to Perovskite on Glass Photovoltaic Modules. *Prog. Photovoltaics Res. Appl.* **2017**, *25*, 390–405. 724
- 725 (11) Wang, R.; Mujahid, M.; Duan, Y.; Wang, Z. K.; Xue, J.; Yang, Y. A Review of Perovskites Solar Cell Stability. *Adv. Funct. Mater.* **2019**, *29*, 1808843. 726
- 727 (12) Domanski, K.; Correa-Baena, J.-P.; Mine, N.; Nazeeruddin, M. K.; Abate, A.; Saliba, M.; Tress, W.; Hagfeldt, A.; Grätzel, M. Not All That Glitters Is Gold: Metal-Migration-Induced Degradation in Perovskite Solar Cells. *ACS Nano* **2016**, *10*, 6306–6314. 728
- 729 (13) Shi, L.; Bucknall, M. P.; Young, T. L.; Zhang, M.; Hu, L.; Bing, J.; Lee, D. S.; Kim, J.; Wu, T.; Takamura, N.; McKenzie, D. R.; Huang, S.; Green, M. A.; Ho-Baillie, A. W. Y. Gas chromatography-mass spectrometry analyses of encapsulated stable perovskite solar cells. *Science* **2020**, *368*, No. eaba2412. 730
- 731 (14) Li, Z.; Zhao, Y.; Wang, X.; Sun, Y.; Zhao, Z.; Li, Y.; Zhou, H.; Chen, Q. Cost Analysis of Perovskite Tandem Photovoltaics. *Joule* **2018**, *2*, 1559–1572. 732
- 733 (15) EPA. *Levelized Cost and Levelized Avoided Cost of New Generation Resources in the Annual Energy Outlook 2020*, U.S. EIA Lcoe, 202, 2020. 734

- 756 (16) Fagiolari, L.; Bella, F. Carbon-Based Materials for Stable,
757 Cheaper and Large-Scale Processable Perovskite Solar Cells. *Energy*
758 *Environ. Sci.* **2019**, *12*, 3437–3472.
- 759 (17) Bogachuk, D.; Zouhair, S.; Wojciechowski, K.; Yang, B.; Babu,
760 V.; Wagner, L.; Xu, B.; Lim, J.; Mastroianni, S.; Pettersson, H.;
761 Hagfeldt, A.; Hinsch, A. Low-Temperature Carbon-Based Electrodes
762 in Perovskite Solar Cells. *Energy Environ. Sci.* **2020**, *13*, 3880–3916.
- 763 (18) Wagner, L.; Mastroianni, S.; Hinsch, A. Reverse Manufacturing
764 Enables Perovskite Photovoltaics to Reach the Carbon Footprint
765 Limit of a Glass Substrate. *Joule* **2020**, *4*, 882–901.
- 766 (19) Ku, Z.; Rong, Y.; Xu, M.; Liu, T.; Han, H. Full Printable
767 Processed Mesoscopic CH₃NH₃PbI₃/TiO₂ Heterojunction Solar
768 Cells with Carbon Counter Electrode. *Sci. Rep.* **2013**, *3*, 3132.
- 769 (20) Grancini, G.; Roldán-Carmona, C.; Zimmermann, I.; Mosconi,
770 E.; Lee, X.; Martineau, D.; Narbey, S.; Oswald, F.; De Angelis, F.;
771 Graetzel, M.; Nazeeruddin, M. K. One-Year Stable Perovskite Solar
772 Cells by 2D/3D Interface Engineering. *Nat. Commun.* **2017**, *8*, 15684.
- 773 (21) Wei, Z.; Yan, K.; Chen, H.; Yi, Y.; Zhang, T.; Long, X.; Li, J.;
774 Zhang, L.; Wang, J.; Yang, S. Cost-Efficient Clamping Solar Cells
775 Using Candle Soot for Hole Extraction from Ambipolar Perovskites.
776 *Energy Environ. Sci.* **2014**, *7*, 3326–3333.
- 777 (22) Wei, Z.; Chen, H.; Yan, K.; Yang, S. Inkjet Printing and Instant
778 Chemical Transformation of a CH₃NH₃PbI₃/Nanocarbon Electrode
779 and Interface for Planar Perovskite Solar Cells. *Angew. Chem. Int. Ed.*
780 **2014**, *53*, 13239–13243.
- 781 (23) Zhang, F.; Yang, X.; Wang, H.; Cheng, M.; Zhao, J.; Sun, L.
782 Structure Engineering of Hole-Conductor Free Perovskite-Based
783 Solar Cells with Low-Temperature-Processed Commercial Carbon
784 Paste As Cathode. *ACS Appl. Mater. Interfaces* **2014**, *6*, 16140–16146.
- 785 (24) Yang, Y.; Xiao, J.; Wei, H.; Zhu, L.; Li, D.; Luo, Y.; Wu, H.;
786 Meng, Q. An All-Carbon Counter Electrode for Highly Efficient
787 Hole-Conductor-Free Organo-Metal Perovskite Solar Cells. *RSC Adv.*
788 **2014**, *4*, 52825–52830.
- 789 (25) Chen, H.; Yang, S. Carbon-Based Perovskite Solar Cells
790 without Hole Transport Materials: The Front Runner to the Market?
791 *Adv. Mater.* **2017**, *29*, 1603994.
- 792 (26) Mei, A.; Li, X.; Liu, L.; Ku, Z.; Liu, T.; Rong, Y.; Xu, M.; Hu,
793 M.; Chen, J.; Yang, Y.; Gratzel, M.; Han, H. A Hole-Conductor-Free,
794 Fully Printable Mesoscopic Perovskite Solar Cell with High Stability.
795 *Science* **2014**, *345*, 295–298.
- 796 (27) Zhou, H.; Shi, Y.; Dong, Q.; Zhang, H.; Xing, Y.; Wang, K.; Du,
797 Y.; Ma, T. Hole-Conductor-Free, Metal-Electrode-Free TiO₂/
798 CH₃NH₃PbI₃ Heterojunction Solar Cells Based on a Low-Temper-
799 ature Carbon Electrode. *J. Phys. Chem. Lett.* **2014**, *5*, 3241–3246.
- 800 (28) Maniarasu, S.; Korukonda, T. B.; Manjunath, V.; Ramasamy, E.;
801 Ramesh, M.; Veerappan, G. Recent Advancement in Metal Cathode
802 and Hole-Conductor-Free Perovskite Solar Cells for Low-Cost and
803 High Stability: A Route towards Commercialization. *Renew. Sustain.*
804 *Energy Rev.* **2018**, *82*, 845–857.
- 805 (29) Zhou, J.; Wu, J.; Li, N.; Li, X.; Zheng, Y.-Z.; Tao, X. Efficient
806 All-Air Processed Mixed Cation Carbon-Based Perovskite Solar Cells
807 with Ultra-High Stability. *J. Mater. Chem. A* **2019**, *7*, 17594–17603.
- 808 (30) Aitola, K.; Sveinbjörnsson, K.; Correa-Baena, J.-P.; Kaskela, A.;
809 Abate, A.; Tian, Y.; Johansson, E. M. J.; Grätzel, M.; Kauppinen, E. I.;
810 Hagfeldt, A.; Boschloo, G. Carbon Nanotube-Based Hybrid Hole-
811 Transporting Material and Selective Contact for High Efficiency
812 Perovskite Solar Cells. *Energy Environ. Sci.* **2016**, *9*, 461–466.
- 813 (31) Jeon, I.; Shawky, A.; Seo, S.; Qian, Y.; Anisimov, A.;
814 Kauppinen, E. I.; Matsuo, Y.; Maruyama, S. Carbon Nanotubes to
815 Outperform Metal Electrodes in Perovskite Solar Cells via Dopant
816 Engineering and Hole-Selectivity Enhancement. *J. Mater. Chem. A*
817 **2020**, *8*, 11141–11147.
- 818 (32) Yang, Y.; Chen, H.; Hu, C.; Yang, S. Polyethyleneimine-
819 Functionalized Carbon Nanotubes as an Interlayer to Bridge
820 Perovskite/Carbon for All Inorganic Carbon-Based Perovskite Solar
821 Cells. *J. Mater. Chem. A* **2019**, *7*, 22005–22011.
- 822 (33) Wang, Y.; Zhao, H.; Mei, Y.; Liu, H.; Wang, S.; Li, X. Carbon
823 Nanotube Bridging Method for Hole Transport Layer-Free Paintable
Carbon-Based Perovskite Solar Cells. *ACS Appl. Mater. Interfaces* **2020**, *11*, 916–923.
- (34) C Carbon Nanotube (CNT) Market 2020. *Covid-19 Impact*
Analysis, Top Trends, Size, Scope, Statistical Analysis and Forecast to
2024, 2020.
- (35) Zhang, H.; Xiao, J.; Shi, J.; Su, H.; Luo, Y.; Li, D.; Wu, H.;
Cheng, Y.-B.; Meng, Q. Self-Adhesive Macroporous Carbon Electrodes for Efficient and Stable Perovskite Solar Cells. *Adv. Funct. Mater.* **2018**, *28*, 1802985.
- (36) Gholipour, S.; Correa-Baena, J.-P.; Domanski, K.; Matsui, T.;
Steier, L.; Giordano, F.; Tajabadi, F.; Tress, W.; Saliba, M.; Abate, A.;
Morteza Ali, A.; Taghavinia, N.; Grätzel, M.; Hagfeldt, A. Highly
Efficient and Stable Perovskite Solar Cells Based on a Low-Cost
Carbon Cloth. *Adv. Energy Mater.* **2016**, *6*, 1601116.
- (37) Yang, Y.; Hoang, M. T.; Yao, D.; Pham, N. D.; Tiong, V. T.;
Wang, X.; Sun, W.; Wang, H. High Performance Carbon-Based Planar
Perovskite Solar Cells by Hot-Pressing Approach. *Sol. Energy Mater. Sol. Cells* **2020**, *210*, 110517.
- (38) Spyropoulos, G. D.; Ramirez Quiroz, C. O.; Salvador, M.; Hou,
Y.; Gasparini, N.; Schweizer, P.; Adams, J.; Kubis, P.; Li, N.; Spiecker,
E.; Ameri, T.; Egelhaaf, H.-J.; Brabec, C. J. Organic and Perovskite
Solar Modules Innovated by Adhesive Top Electrode and Depth-
Resolved Laser Patterning. *Energy Environ. Sci.* **2016**, *9*, 2302–2313.
- (39) Su, H.; Xiao, J.; Li, Q.; Peng, C.; Zhang, X.; Mao, C.; Yao, Q.;
Lu, Y.; Ku, Z.; Zhong, J.; Li, W.; Peng, Y.; Huang, F.; Cheng, Y.
Carbon Film Electrode Based Square-Centimeter Scale Planar
Perovskite Solar Cells Exceeding 17% Efficiency. *Mater. Sci. Semicond. Process.* **2020**, *107*, 104809.
- (40) Hu, Y.; Si, S.; Mei, A.; Rong, Y.; Liu, H.; Li, X.; Han, H. Stable
Large-Area (10×10 cm²) Printable Mesoscopic Perovskite Module
Exceeding 10% Efficiency. *Sol. RRL* **2017**, *1*, 1600019.
- (41) Priyadarshi, A.; Haur, L. J.; Murray, P.; Fu, D.; Kulkarni, S.;
Xing, G.; Sum, T. C.; Mathews, N.; Mhaisalkar, S. G. A Large Area
(70 Cm²) Monolithic Perovskite Solar Module with a High Efficiency
and Stability. *Energy Environ. Sci.* **2016**, *9*, 3687–3692.
- (42) Cai, L.; Liang, L.; Wu, J.; Ding, B.; Gao, L.; Fan, B. Large Area
Perovskite Solar Cell Module. *J. Semicond.* **2017**, *38*, 014006.
- (43) Li, Z.; Klein, T. R.; Kim, D. H.; Yang, M.; Berry, J. J.; van Hest,
M. F. A. M.; Zhu, K. Scalable Fabrication of Perovskite Solar Cells.
Nat. Rev. Mater. **2018**, *3*, 18017.
- (44) Meroni, S. M. P.; Hooper, K. E. A.; Dunlop, T.; Baker, J. A.;
Worsley, D.; Charbonneau, C.; Watson, T. M. Scribing Method for
Carbon Perovskite Solar Modules. *Energies* **2020**, *13*, 1589.
- (45) Qiu, L.; He, S.; Ono, L. K.; Liu, S.; Qi, Y. Scalable Fabrication
of Metal Halide Perovskite Solar Cells and Modules. *ACS Energy Lett.* **2019**, *4*, 2147–2167.
- (46) Chu, Q.-Q.; Ding, B.; Peng, J.; Shen, H.; Li, X.; Liu, Y.; Li, C.-
X.; Li, C.-J.; Yang, G.-J.; White, T. P.; Catchpole, K. R. Highly Stable
Carbon-Based Perovskite Solar Cell with a Record Efficiency of over
18% via Hole Transport Engineering. *J. Mater. Sci. Technol.* **2019**, *35*,
987–993.
- (47) Wu, M.; Sun, M.; Zhou, H.; Ma, J. Y.; Ma, T. Carbon Counter
Electrodes in Dye-Sensitized and Perovskite Solar Cells. *Adv. Funct. Mater.* **2020**, *30*, 1906451.
- (48) Dou, B.; Whitaker, J. B.; Bruening, K.; Moore, D. T.; Wheeler,
L. M.; Ryter, J.; Breslin, N. J.; Berry, J. J.; Garner, S. M.; Barnes, F. S.;
Shaheen, S. E.; Tassone, C. J.; Zhu, K.; van Hest, M. F. A. M. Roll-to-
Roll Printing of Perovskite Solar Cells. *ACS Energy Lett.* **2018**, *3*,
2558–2565.
- (49) Galagan, Y.; Di Giacomo, F.; Gortler, H.; Kirchner, G.; de Vries,
I.; Andriessen, R.; Groen, P. Roll-to-Roll Slot Die Coated Perovskite
for Efficient Flexible Solar Cells. *Adv. Energy Mater.* **2018**, *8*, 1801935.
- (50) Taheri, B.; Yaghoobi Nia, N.; Agresti, A.; Pescetelli, S.;
Ciceroni, C.; Del Rio Castillo, A. E.; Cinà, L.; Bellani, S.; Bonaccorso,
F.; Di Carlo, A. Graphene-Engineered Automated Sprayed Meso-
scopic Structure for Perovskite Device Scaling-Up. *2D Mater.* **2018**, *5*,
045034.
- (51) Lamanna, E.; Matteocci, F.; Calabrò, E.; Serenelli, L.; Salza, E.;
Martini, L.; Menchini, F.; Izzì, M.; Agresti, A.; Pescetelli, S.; Bellani,

- 893 S.; Del Río Castillo, A. E.; Bonaccorso, F.; Tucci, M.; Di Carlo, A.
894 Mechanically Stacked, Two-Terminal Graphene-Based Perovskite/
895 Silicon Tandem Solar Cell with Efficiency over 26%. *Joule* **2020**, *4*,
896 865–881.
- 897 (52) Agresti, A.; Pescetelli, S.; Palma, A. L.; Martín-García, B.;
898 Najafi, L.; Bellani, S.; Moreels, L.; Prato, M.; Bonaccorso, F.; Di Carlo,
899 A. Two-Dimensional Material Interface Engineering for Efficient
900 Perovskite Large-Area Modules. *ACS Energy Lett.* **2019**, *4*, 1862–
901 1871.
- 902 (53) Raptis, D.; Stoichkov, V.; Meroni, S. M. P.; Pockett, A.;
903 Worsley, C. A.; Carnie, M.; Worsley, D. A.; Watson, T. Enhancing
904 Fully Printable Mesoscopic Perovskite Solar Cell Performance Using
905 Integrated Metallic Grids to Improve Carbon Electrode Conductivity.
906 *Curr. Appl. Phys.* **2020**, *20*, 619–627.
- 907 (54) Chen, H.; Wei, Z.; He, H.; Zheng, X.; Wong, K. S.; Yang, S.
908 Solvent Engineering Boosts the Efficiency of Paintable Carbon-Based
909 Perovskite Solar Cells to Beyond 14%. *Adv. Energy Mater.* **2016**, *6*,
910 1502087.
- 911 (55) Bashir, A.; Shukla, S.; Lew, J. H.; Shukla, S.; Bruno, A.; Gupta,
912 D.; Baikie, T.; Patidar, R.; Akhter, Z.; Priyadarshi, A.; Mathews, N.;
913 Mhaisalkar, S. G. Spinel Co₃O₄ nanomaterials for efficient and stable
914 large area carbon-based printed perovskite solar cells. *Nanoscale* **2018**,
915 *10*, 2341–2350.
- 916 (56) Bashir, A.; Lew, J. H.; Shukla, S.; Gupta, D.; Baikie, T.;
917 Chakraborty, S.; Patidar, R.; Bruno, A.; Mhaisalkar, S.; Akhter, Z. Cu-
918 Doped Nickel Oxide Interface Layer with Nanoscale Thickness for
919 Efficient and Highly Stable Printable Carbon-Based Perovskite Solar
920 Cell. *Sol. Energy* **2019**, *182*, 225–236.
- 921 (57) Liu, Z.; Sun, B.; Shi, T.; Tang, Z.; Liao, G. Enhanced
922 Photovoltaic Performance and Stability of Carbon Counter Electrode
923 Based Perovskite Solar Cells Encapsulated by PDMS. *J. Mater. Chem.*
924 *A* **2016**, *4*, 10700–10709.
- 925 (58) Babu, V.; Fuentes Pineda, R.; Ahmad, T.; Alvarez, A. O.;
926 Castriotta, L. A.; Di Carlo, A.; Fabregat-Santiago, F.; Wojciechowski,
927 K. Improved Stability of Inverted and Flexible Perovskite Solar Cells
928 with Carbon Electrode. *ACS Appl. Energy Mater.* **2020**, *3*, 5126–5134.
- 929 (59) Meng, F.; Gao, L.; Yan, Y.; Cao, J.; Wang, N.; Wang, T.; Ma, T.
930 Ultra-Low-Cost Coal-Based Carbon Electrodes with Seamless
931 Interfacial Contact for Effective Sandwich-Structured Perovskite
932 Solar Cells. *Carbon* **2019**, *145*, 290–296.
- 933 (60) Zhang, C.; Wang, S.; Zhang, H.; Feng, Y.; Tian, W.; Yan, Y.;
934 Bian, J.; Wang, Y.; Jin, S.; Zakeeruddin, S. M.; Grätzel, M.; Shi, Y.
935 Efficient Stable Graphene-Based Perovskite Solar Cells with High
936 Flexibility in Device Assembling via Modular Architecture Design.
937 *Energy Environ. Sci.* **2019**, *12*, 3585–3594.
- 938 (61) Bowring, A. R.; Bertoluzzi, L.; O'Regan, B. C.; McGehee, M. D.
939 Reverse Bias Behavior of Halide Perovskite Solar Cells. *Adv. Energy*
940 *Mater.* **2018**, *8*, 1702365.
- 941 (62) Razera, R. A. Z.; Jacobs, D. A.; Fu, F.; Fiala, P.; Dusouillez, M.;
942 Sahli, F.; Yang, T. C. J.; Ding, L.; Walter, A.; Feil, A. F.; Boudinov, H.
943 I.; Nicolay, S.; Ballif, C.; Jeangros, Q. Instability of p-i-n perovskite
944 solar cells under reverse bias. *J. Mater. Chem. A* **2020**, *8*, 242–250.
- 945 (63) <https://bedimensional.com/> (data accessed on 12 April, 2021).
- 946 (64) Del Rio-Castillo, A. E.; Ansaldo, A.; Pellegrini, V.; Bonaccorso,
947 F. Exfoliation Materials by Wet-Jet Milling Techniques. WO
948 2017089987 A1, 2017.
- 949 (65) Del Rio Castillo, A. E.; Pellegrini, V.; Ansaldo, A.; Ricciardella,
950 F.; Sun, H.; Marasco, L.; Buha, J.; Dang, Z.; Gagliani, L.; Lago, E.;
951 Curreli, N.; Gentiluomo, S.; Palazon, F.; Prato, M.; Oropesa-Nuñez,
952 R.; Toth, P. S.; Mantero, E.; Crugliano, M.; Gamucci, A.; Tomadin,
953 A.; Polini, M.; Bonaccorso, F. High-Yield Production of 2D Crystals
954 by Wet-Jet Milling. *Mater. Horiz.* **2018**, *5*, 890–904.
- 955 (66) Garakani, M. A.; Bellani, S.; Pellegrini, V.; Oropesa-Nuñez, R.;
956 Castillo, A. E. D. R.; Abouali, S.; Najafi, L.; Martín-García, B.;
957 Ansaldo, A.; Bondavalli, P.; Demirci, C.; Romano, V.; Mantero, E.;
958 Marasco, L.; Prato, M.; Bracciale, G.; Bonaccorso, F. Scalable Spray-
959 Coated Graphene-Based Electrodes for High-Power Electrochemical
960 Double-Layer Capacitors Operating over a Wide Range of Temper-
961 ature. *Energy Storage Mater.* **2021**, *34*, 1–11.
- (67) Kong, W.; Kum, H.; Bae, S.-H.; Shim, J.; Kim, H.; Kong, L.; 962
Meng, Y.; Wang, K.; Kim, C.; Kim, J. Path towards Graphene 963
Commercialization from Lab to Market. *Nat. Nanotechnol.* **2019**, *14*, 964
927–938. 965
- (68) Zhu, Y.; Murali, S.; Cai, W.; Li, X.; Suk, J. W.; Potts, J. R.; 966
Ruoff, R. S. Graphene and Graphene Oxide: Synthesis, Properties, 967
and Applications. *Adv. Mater.* **2010**, *22*, 3906–3924. 968
- (69) Backes, C.; Abdelkader, A. M.; Alonso, C.; Andrieux-Ledier, A.; 969
Arenal, R.; Azpeitia, J.; Balakrishnan, N.; Banszeru, L.; Barjon, J.; 970
Bartali, R.; Bellani, S.; Berger, C.; Berger, R.; Ortega, M. M. B.; 971
Bernard, C.; Beton, P. H.; Beyer, A.; Bianco, A.; Bøggild, P.; 972
Bonaccorso, F.; Barin, G. B.; Botas, C.; Bueno, R. A.; Carriazo, D.; 973
Castellanos-Gomez, A.; Christian, M.; Ciesielski, A.; Ciuk, T.; Cole, 974
M. T.; Coleman, J.; Coletti, C.; Crema, L.; Cun, H.; Dasler, D.; De 975
Fazio, D.; Díez, N.; Drieschner, S.; Duesberg, G. S.; Fasel, R.; Feng, 976
X.; Fina, A.; Forti, S.; Galiotis, C.; Garberoglu, G.; García, J. M.; 977
Garrido, J. A.; Gibertini, M.; Götzhäuser, A.; Gómez, J.; Greber, T.; 978
Hauke, F.; Hemmi, A.; Hernandez-Rodriguez, I.; Hirsch, A.; Hodge, 979
S. A.; Huttel, Y.; Jepsen, P. U.; Jimenez, I.; Kaiser, U.; Kaplas, T.; Kim, 980
H.; Kis, A.; Papagelis, K.; Kostarelos, K.; Krajewska, A.; Lee, K.; Li, 981
C.; Lipsanen, H.; Liscio, A.; Lohe, M. R.; Loiseau, A.; Lombardi, L.; 982
Francisca López, M.; Martin, O.; Martín, C.; Martínez, L.; Martín- 983
Gago, J. A.; Ignacio Martínez, J.; Marzari, N.; Mayoral, A.; McManus, 984
J.; Melucci, M.; Méndez, J.; Merino, C.; Merino, P.; Meyer, A. P.; 985
Miniussi, E.; Miseikis, V.; Mishra, N.; Morandi, V.; Munuera, C.; 986
Muñoz, R.; Nolan, H.; Ortolani, L.; Ott, A. K.; Palacio, I.; Palermo, 987
V.; Parthenios, J.; Pasternak, L.; Patane, A.; Prato, M.; Prevost, H.; 988
Prudkovskiy, V.; Pugno, N.; Rojo, T.; Rossi, A.; Ruffieux, P.; Samori, 989
P.; Schué, L.; Setijadi, E.; Seyller, T.; Speranza, G.; Stampfer, C.; 990
Stenger, I.; Strupinski, W.; Svirko, Y.; Taioli, S.; Teo, K. B. K.; Testi, 991
M.; Tomarchio, F.; Tortello, M.; Treossi, E.; Turchanin, A.; Yazquez, 992
E.; Villaro, E.; Whelan, P. R.; Xia, Z.; Yakimova, R.; Yang, S.; Yazdi, G. 993
R.; Yim, C.; Yoon, D.; Zhang, X.; Zhuang, X.; Colombo, L.; Ferrari, A. 994
C.; Garcia-Hernandez, M. Production and Processing of Graphene 995
and Related Materials. *2D Mater.* **2020**, *7*, 022001. 996
- (70) Ni, Z. H.; Ponomarenko, L. A.; Nair, R. R.; Yang, R.; 997
Anissimova, S.; Grigorieva, I. V.; Schedin, F.; Blake, P.; Shen, Z. X.; 998
Hill, E. H.; Novoselov, K. S.; Geim, A. K. On Resonant Scatterers As a 999
Factor Limiting Carrier Mobility in Graphene. *Nano Lett.* **2010**, *10*,
1000 3868–3872. 1001
- (71) Mattevi, C.; Eda, G.; Agnoli, S.; Miller, S.; Mkhoyan, K. A.; 1002
Celik, O.; Mastrogianni, D.; Granozzi, G.; Garfunkel, E.; 1003
Chhowalla, M. Evolution of Electrical, Chemical, and Structural 1004
Properties of Transparent and Conducting Chemically Derived 1005
Graphene Thin Films. *Adv. Funct. Mater.* **2009**, *19*, 2577–2583. 1006
- (72) Liang, L.; Cai, Y.; Li, X.; Nazeeruddin, M. K.; Gao, P. All That 1007
Glitters Is Not Gold: Recent Progress of Alternative Counter 1008
Electrodes for Perovskite Solar Cells. *Nano Energy* **2018**, *52*, 211–
1009 238. 1010
- (73) Girolami, M.; Bellucci, A.; Mastellone, M.; Serpente, V.; 1011
Orlando, S.; Valentini, V.; Palma, A. L.; Di Carlo, A.; Trucchi, D. M. 1012
Improving the Performance of Printable Carbon Electrodes by 1013
Femtosecond Laser Treatment. C—*J. Carbon Res.* **2020**, *6*, 48. 1014
- (74) Wolf, M.; Rauschenbach, H. Series Resistance Effects on Solar 1015
Cell Measurements. *Adv. Energy Convers.* **1963**, *3*, 455–479. 1016
- (75) Choi, S.; Potscavage, W. J.; Kippelen, B. Area-Scaling of 1017
Organic Solar Cells. *J. Appl. Phys.* **2009**, *106*, 054507. 1018
- (76) International Electrotechnical Commission. *Terrestrial Photo-* 1019
voltatic (PV) Modules—Design Qualification and Type Approval—Part 1020
1: Test Requirements. Iec 61215, 2016. 1021
- (77) Miller, D. C.; Alharbi, F.; Andreas, A.; Bokria, J. G.; Burns, D. 1022
M.; Bushong, J.; Chen, X.; Dietz, D.; Fowler, S.; Gu, X.; Habte, A.; 1023
Honeker, C. C.; Kempe, M. D.; Khonkar, H.; Köhl, M.; Phillips, N. 1024
H.; Rivera, J.; Scott, K. P.; Singh, A.; Zielnik, A. F. Degradation in 1025
Photovoltaic Encapsulation Strength of Attachment: Results of the 1026
First PVQAT TG5 Artificial Weathering Study. *Prog. Photovoltaics* 1027
Res. Appl. **2020**, *28*, 639–658. 1028
- (78) Checharoen, R.; Rolston, N.; Harwood, D.; Bush, K. A.; 1029
Dauskardt, R. H.; McGehee, M. D. Design and Understanding of 1030

- 1031 Encapsulated Perovskite Solar Cells to Withstand Temperature
1032 Cycling. *Energy Environ. Sci.* **2018**, *11*, 144–150.
- 1033 (79) Saliba, M.; Matsui, T.; Seo, J.-Y.; Domanski, K.; Correa-Baena,
1034 J.-P.; Nazeeruddin, M. K.; Zakeeruddin, S. M.; Tress, W.; Abate, A.;
1035 Hagfeldt, A.; Grätzel, M. Cesium-Containing Triple Cation Perovskite
1036 Solar Cells: Improved Stability, Reproducibility and High Efficiency.
1037 *Energy Environ. Sci.* **2016**, *9*, 1989–1997.
- 1038 (80) Shariatinia, Z. Recent Progress in Development of Diverse
1039 Kinds of Hole Transport Materials for the Perovskite Solar Cells: A
1040 Review. *Renew. Sustain. Energy Rev.* **2020**, *119*, 109608.
- 1041 (81) Pashaei, B.; Bellani, S.; Shahroosvand, H.; Bonaccorso, F.
1042 Molecularly Engineered Hole-Transport Material for Low-Cost
1043 Perovskite Solar Cells. *Chem. Sci.* **2020**, *11*, 2429–2439.
- 1044 (82) Biccari, F.; Gabelloni, F.; Burzi, E.; Gurioli, M.; Pescetelli, S.;
1045 Agresti, A.; Del Rio Castillo, A. E.; Ansaldo, A.; Kymakis, E.;
1046 Bonaccorso, F.; Di Carlo, A.; Vinattieri, A. Graphene-Based Electron
1047 Transport Layers in Perovskite Solar Cells: A Step-Up for an Efficient
1048 Carrier Collection. *Adv. Energy Mater.* **2017**, *7*, 1701349.
- 1049 (83) O’Keeffe, P.; Catone, D.; Paladini, A.; Toschi, F.; Turchini, S.;
1050 Avaldi, L.; Martelli, F.; Agresti, A.; Pescetelli, S.; Del Rio Castillo, A.
1051 E.; Bonaccorso, F.; Di Carlo, A. Graphene-Induced Improvements of
1052 Perovskite Solar Cell Stability: Effects on Hot-Carriers. *Nano Lett.*
1053 **2019**, *19*, 684–691.
- 1054 (84) Najafi, L.; Taheri, B.; Martín-García, B.; Bellani, S.; Di
1055 Girolamo, D.; Agresti, A.; Oropesa-Nuñez, R.; Pescetelli, S.; Vesce, L.;
1056 Calabrò, E.; Prato, M.; Del Rio Castillo, A. E.; Di Carlo, A.;
1057 Bonaccorso, F. MoS₂ Quantum Dot/Graphene Hybrids for Advanced
1058 Interface Engineering of a CH₃NH₃PbI₃ Perovskite Solar Cell with
1059 an Efficiency of over 20. *ACS Nano* **2018**, *12*, 10736–10754.
- 1060 (85) Capasso, A.; Matteocci, F.; Najafi, L.; Prato, M.; Buha, J.; Cinà,
1061 L.; Pellegrini, V.; Carlo, A. D.; Bonaccorso, F. Few-Layer MoS₂Flakes
1062 as Active Buffer Layer for Stable Perovskite Solar Cells. *Adv. Energy*
1063 *Mater.* **2016**, *6*, 1600920.
- 1064 (86) Saliba, M.; Correa-Baena, J.-P.; Wolff, C. M.; Stolterfoht, M.;
1065 Phung, N.; Albrecht, S.; Neher, D.; Abate, A. How to Make over 20%
1066 Efficient Perovskite Solar Cells in Regular (n-i-p) and Inverted (p-i-n)
1067 Architectures. *Chem. Mater.* **2018**, *30*, 4193–4201.
- 1068 (87) Mette, A. New Concepts for Front Side Metallization of
1069 Industrial Silicon Solar Cells. Ph.D. Thesis, Fraunhofer-Institut für
1070 Solare Energiesysteme Freiburg im Breisgau, 2007.
- 1071 (88) Descoeur, A.; Allebé, C.; Badel, N.; Barraud, L.;
1072 Champlaud, J.; Christmann, G.; Debrot, F.; Faes, A.; Geissbühler,
1073 J.; Horzel, J.; Lachowicz, A.; Levrat, J.; Martin de Nicolas, S.; Nicolay,
1074 S.; Paviet-Salomon, B.; Senaud, L.-L.; Ballif, C.; Despeisse, M. Low-
1075 Temperature Processes for Passivation and Metallization of High-
1076 Efficiency Crystalline Silicon Solar Cells. *Sol. Energy* **2018**, *175*, 54–
1077 59.
- 1078 (89) Agresti, A.; Pescetelli, S.; Palma, A. L.; Del Rio Castillo, A. E.;
1079 Konios, D.; Kakavelakis, G.; Razza, S.; Cinà, L.; Kymakis, E.;
1080 Bonaccorso, F.; Di Carlo, A. Graphene Interface Engineering for
1081 Perovskite Solar Modules: 12.6% Power Conversion Efficiency over
1082 50 Cm² Active Area. *ACS Energy Lett.* **2017**, *2*, 279–287.
- 1083 (90) Khenkin, M. V.; Katz, E. A.; Abate, A.; Bardizza, G.; Berry, J. J.;
1084 Brabec, C.; Brunetti, F.; Bulović, V.; Burlingame, Q.; Di Carlo, A.;
1085 Checharoen, R.; Cheng, Y.-B.; Colsmann, A.; Cros, S.; Domanski, K.;
1086 Dusza, M.; Fell, C. J.; Forrest, S. R.; Galagan, Y.; Di Girolamo, D.;
1087 Grätzel, M.; Hagfeldt, A.; von Hauff, E.; Hoppe, H.; Kettle, J.; Köbler,
1088 H.; Leite, M. S.; Liu, S.; Loo, Y.-L.; Luther, J. M.; Ma, C.-Q.; Madsen,
1089 M.; Manceau, M.; Matheron, M.; McGehee, M.; Meitzner, R.;
1090 Nazeeruddin, M. K.; Nogueira, A. F.; Odabaşı, Ç.; Osherov, A.; Park,
1091 N.-G.; Reese, M. O.; De Rossi, F.; Saliba, M.; Schubert, U. S.; Snaith,
1092 H. J.; Stranks, S. D.; Tress, W.; Troshin, P. A.; Turkovic, V.; Veestra,
1093 S.; Visoly-Fisher, I.; Walsh, A.; Watson, T.; Xie, H.; Yildirim, R.;
1094 Zakeeruddin, S. M.; Zhu, K.; Lira-Cantu, M. Consensus Statement for
1095 Stability Assessment and Reporting for Perovskite Photovoltaics
1096 Based on ISOS Procedures. *Nat. Energy* **2020**, *5*, 35–49.
- 1097 (91) Calabrò, E.; Matteocci, F.; Paci, B.; Cinà, L.; Vesce, L.;
1098 Barichello, J.; Generosi, A.; Reale, A.; Di Carlo, A. Easy Strategy to
1099 Enhance Thermal Stability of Planar PSCs by Perovskite Defect
Passivation and Low-Temperature Carbon-Based Electrode. *ACS Appl. Mater. Interfaces* **2020**, *12*, 32536–32547.
- (92) Zhu, W.; Zhang, Z.; Chai, W.; Chen, D.; Xi, H.; Chang, J.;
Zhang, J.; Zhang, C.; Hao, Y. Benign Pinholes in CsPbI₂Br₂ Absorber
Film Enable Efficient Carbon-Based, All-Inorganic Perovskite Solar
Cells. *ACS Appl. Energy Mater.* **2019**, *2*, 5254–5262.
- (93) Ryu, J.; Lee, K.; Yun, J.; Yu, H.; Lee, J.; Jang, J. Paintable
Carbon-Based Perovskite Solar Cells with Engineered Perovskite/
Carbon Interface Using Carbon Nanotubes Dripping Method. *Small*
2017, *13*, 1701225.
- (94) Liu, T.; Wang, Z.; Lou, L.; Xiao, S.; Zheng, S.; Yang, S.
Interfacial Post-Treatment for Enhancing the Performance of
Printable Carbon-Based Perovskite Solar Cells. *Sol. RRL* **2020**, *4*,
1900278.
- (95) Kim, J.; Lee, G.; Lee, K.; Yu, H.; Lee, J. W.; Yoon, C.-M.; Kim,
S. G.; Kim, S. K.; Jang, J. Fluorine Plasma Treatment on Carbon-
Based Perovskite Solar Cells for Rapid Moisture Protection Layer
Formation and Performance Enhancement. *Chem. Commun.* **2020**, *56*,
535–538.
- (96) Liu, X.; Li, J.; Liu, Z.; Tan, X.; Sun, B.; Xi, S.; Shi, T.; Tang, Z.;
Liao, G. Vapor-assisted deposition of CsPbI₂Br₂ films for highly
efficient and stable carbon-based planar perovskite solar cells with
superior Voc. *Electrochim. Acta* **2020**, *330*, 135266.
- (97) Armin, A.; Habsch, M.; Wolfer, P.; Jin, H.; Li, J.; Shi, Z.;
Burn, P. L.; Meredith, P. Efficient, Large Area, and Thick Junction
Polymer Solar Cells with Balanced Mobilities and Low Defect
Densities. *Adv. Energy Mater.* **2015**, *5*, 1401221.
- (98) Jin, H.; Pivrikas, A.; Lee, K. H.; Aljada, M.; Habsch, M.; Burn,
P. L.; Meredith, P. Factors Influencing the Efficiency of Current
Collection in Large Area, Monolithic Organic Solar Cells. *Adv. Energy*
Mater. **2012**, *2*, 1338–1342.
- (99) Meredith, P.; Armin, A. Scaling of next Generation Solution
Processed Organic and Perovskite Solar Cells. *Nat. Commun.* **2018**, *9*,
5261.
- (100) Kim, D. H.; Whitaker, J. B.; Li, Z.; van Hest, M. F. A. M.; Zhu,
K. Outlook and Challenges of Perovskite Solar Cells toward Terawatt-
Scale Photovoltaic Module Technology. *Joule* **2018**, *2*, 1437–1451.
- (101) Haas, S.; Krumscheid, S.; Bauer, A.; Lambert, A.; Rau, U.
Novel Series Connection Concept for Thin Film Solar Modules. *Prog.*
Photovoltaics Res. Appl. **2013**, *21*, 972–979.
- (102) Westin, P.-O.; Zimmermann, U.; Edoff, M. Laser Patterning of
P2 Interconnect via in Thin-Film CIGS PV Modules. *Sol. Energy*
Mater. Sol. Cells **2008**, *92*, 1230–1235.
- (103) Booth, H. Laser Processing in Industrial Solar Module
Manufacturing. *J. Laser Micro/Nanoeng.* **2010**, *5*, 183–191.
- (104) Werner, J.; Boyd, C. C.; Moot, T.; Wolf, E. J.; France, R. M.;
Johnson, S. A.; van Hest, M. F. A. M.; Luther, J. M.; Zhu, K.; Berry, J.
J.; McGehee, M. D. Learning from Existing Photovoltaic Tech-
nologies to Identify Alternative Perovskite Module Designs. *Energy*
Environ. Sci. **2020**, *13*, 3393–3403.
- (105) Kaushika, N.; Rai, A. An Investigation of Mismatch Losses in
Solar Photovoltaic Cell Networks. *Energy* **2007**, *32*, 755–759.
- (106) Patel, H.; Agarwal, V. MATLAB-Based Modeling to Study the
Effects of Partial Shading on PV Array Characteristics. *IEEE Trans.*
Energy Convers. **2008**, *23*, 302–310.
- (107) Moon, S.-J.; Yum, J.-H.; Lofgren, L.; Walter, A.; Sansonnens,
L.; Benkhaira, M.; Nicolay, S.; Bailat, J.; Ballif, C. Laser-Scribing
Patterning for the Production of Organometallic Halide Perovskite
Solar Modules. *IEEE J. Photovoltaics* **2015**, *5*, 1087–1092.
- (108) Simon, M.; Meyer, E. L. Detection and Analysis of Hot-Spot
Formation in Solar Cells. *Sol. Energy Mater. Sol. Cells* **2010**, *94*, 106–
113.
- (109) Hudson, J.; Vasilyev, L.; Schmidt, J.; Horner, G. Economic
Impacts and Approaches to Address Hot-Spot Defects in Photovoltaic
Devices. *2010 35th IEEE Photovoltaic Specialists Conference; IEEE*,
2010; pp 001706–001709.
- (110) Qian, J.; Ernst, M.; Walter, D.; Mahmud, M. A.; Hacke, P.;
Weber, K.; Al-Jassim, M.; Blakers, A. Destructive Reverse Bias Pinning
in Perovskite/Silicon Tandem Solar Modules Caused by Perovskite

- 1169 Hysteresis under Dynamic Shading. *Sustainable Energy Fuels* **2020**, *4*,
1170 4067–4075.
- 1171 (111) Pannebakker, B. B.; de Waal, A. C.; van Sark, W. G. J. H. M.
1172 Photovoltaics in the Shade: One Bypass Diode per Solar Cell
1173 Revisited. *Prog. Photovoltaics Res. Appl.* **2017**, *25*, 836–849.
- 1174 (112) Vieira, R. G.; de Araújo, F. M. U.; Dhimish, M.; Guerra, M. I.
1175 S. A Comprehensive Review on Bypass Diode Application on
1176 Photovoltaic Modules. *Energies* **2020**, *13*, 2472.
- 1177 (113) Fertig, F.; Rein, S.; Schubert, M.; Warta, W. Impact Of
1178 Junction Breakdown In Multi-Crystalline Silicon Solar Cells On Hot
1179 Spot Formation And Module Performance. *26th European Photo-*
1180 *voltic Solar Energy Conference and Exhibition*, 2011.
- 1181 (114) Palma, A. L.; Matteocci, F.; Agresti, A.; Pescetelli, S.; Calabro,
1182 E.; Vesce, L.; Christiansen, S.; Schmidt, M.; Di Carlo, A. Laser-
1183 Patterning Engineering for Perovskite Solar Modules With 95%
1184 Aperture Ratio. *IEEE J. Photovoltaics* **2017**, *7*, 1674–1680.
- 1185 (115) Yang, M.; Kim, D. H.; Klein, T. R.; Li, Z.; Reese, M. O.;
1186 Tremolet de Villers, B. J.; Berry, J. J.; van Hest, M. F. A. M.; Zhu, K.
1187 Highly Efficient Perovskite Solar Modules by Scalable Fabrication and
1188 Interconnection Optimization. *ACS Energy Lett.* **2018**, *3*, 322–328.
- 1189 (116) De Rossi, F.; Baker, J. A.; Beynon, D.; Hooper, K. E. A.;
1190 Meroni, S. M. P.; Williams, D.; Wei, Z.; Yasin, A.; Charbonneau, C.;
1191 Jewell, E. H.; Watson, T. M. All Printable Perovskite Solar Modules
1192 with 198 Cm² Active Area and Over 6% Efficiency. *Adv. Mater.*
1193 *Technol.* **2018**, *3*, 1800156.
- 1194 (117) Tepner, S.; Ney, L.; Linse, M.; Lorenz, A.; Pospischil, M.;
1195 Masuri, K.; Clement, F. Screen pattern simulation for an improved
1196 front-side Ag-electrode metallization of Si-solar cells. *Prog. Photo-*
1197 *voltics Res. Appl.* **2020**, *28*, 1054–1062.
- 1198 (118) Choi, S.; Zhou, Y.; Haske, W.; Shim, J. W.; Fuentes-
1199 Hernandez, C.; Kippelen, B. ITO-Free Large-Area Flexible Organic
1200 Solar Cells with an Embedded Metal Grid. *Org. Electron.* **2015**, *17*,
1201 349–354.